Contract No:

This document was prepared in conjunction with work accomplished under Contract No. 89303321CEM000080 with the U.S. Department of Energy (DOE) Office of Environmental Management (EM).

Disclaimer:

Proceedings of the ASME 2022
Pressure Vessels & Piping Conference
PVP2022
July 17-22, 2022, Las Vegas, Nevada, USA

Draft

PVP2022-86164

DATA-DRIVEN STRESS INTENSITY FACTOR SOLUTIONS FOR AXIAL OUTSIDE SURFACE CRACKS IN THICK-WALL CYLINDERS

Xian-Kui Zhu
Materials Technology
Savannah River National Laboratory
Aiken, SC 29808, USA

Jesse B Zhu
Cornell Tech
New York, NY 10044, USA

Andrew Duncan
Materials Technology
Savannah River National Laboratory
Aiken, SC 29808, USA

ABSTRACT:

Crack assessment methods use the linear elastic or elastic-plastic fracture mechanics that requires calculation of stress intensity factor, K, in the fitness for service codes, such as API 579 and ASME BPVC Section XI. For surface cracks in a pressurized cylinder, the K calculation becomes calculating the influence coefficients G0 and G1 of K in those codes. API 579 provided accurate tabular data of G0 and G1 for selected cylinder sizes (t/R_i), crack aspect ratios (a/c), crack depths (a/t), and crack tip locations based on the 3D finite element analyses. For other cylinder or crack sizes, three-parameter interpolations are needed to calculate G0 and G1. Recently, Xu et al. (PVP2014) and (PVP2016) obtained the curve-fit solutions of G0 and G1 for API selected cylinder sizes. For other cylinders, interpolations are still needed to calculate G0 and G1.

To obtain a more general K solution for any thick-wall cylinder and crack sizes, this paper adopts the state-of-the-art machine learning technology to develop data-driven K solutions based on the tabular datasets of G0 and G1 given in API 579 for axial outside semi-elliptical surface cracks in cylinders at the deepest and surface points. The machine learning method utilizes an artificial neural network (ANN), activation function, and optimal learning algorithm to learn and to determine G0 and G1 as a function of the cylinder size (t/R_i), aspect ratio (a/c), and crack depth (a/t) for axial outside surface cracks at the deepest and surface points. The proposed data-driven solutions of G0 and G1 for the axial outside surface cracks are validated by the curve-fit solutions obtained by Xu et al. (PVP2016).

Keywords: stress intensity factor, influence coefficient, curve fit, machine learning, API 579, ASME BPVC

1. INTRODUCTION

Many failures of pressure vessels have been traced to surface cracks. Thus, accurate stress analyses of these surface cracked components are needed for reliable prediction of their crack growth rates and fracture strengths. In the flaw evaluation, all industry fitness-for-service (FFS) codes, such as the American Petroleum Institute (API) 579 [1] and American Society for Mechanical Engineers (ASME) Boiler and Pressure Vessel Code (BPVC) Section XI [2], adopt the linear elastic or elastic-plastic fracture mechanics method that requires the calculation of stress intensity factor, K, for surface cracks of interest. Because of the complexities of surface crack problems, all investigators have used either engineering estimates or approximate analytical methods to obtain the K factor solutions in the engineering critical analysis (ECA) of pressure vessels.

Early engineering estimates of the K factor for surface cracks in pressurized cylinders were made by Underwood [3] and Kobayashi [4] without consideration of the wall thickness effect and by Kobayashi et al. [5] with consideration of the wall thickness effect. The early three-dimensional (3D) finite element analysis (FEA) of the K factor for semi-elliptical surface cracks in pressurized cylinders were performed by McGowan and Raymond [6] and Newman and Raju [7, 8] for a couple of selected cylinder sizes. Ten years later, Wang and Lamber [9] validated the 3D FEA results of the K factor obtained by Raju and Newman [8] for axial outside surface cracks in cylinders and developed a closed-form solution of the K factor for a thin-wall pipe with one inside radius to wall thickness ratio $R_i/t=10$ in reference to the FEA results and using the weight function

This work was produced by Battelle Savannah River Alliance, LLC under Contract No. 89303321CEM000080 with the U.S. Department of Energy. Publisher acknowledges the U.S. Government license to provide public access under the DOE Public Access Plan (http://energy.gov/downloads/doe-public-access-plan).

method. Recently, with the modern FEA simulations, Akhi and Dhar [10] obtained more accurate FEA results of the K factor and verified the accuracy of the FEA data of the K factor obtained by Raju and Neman [8].

To estimate the K factor for an axial surface crack in a thick-wall cylinder subject to an arbitrarily distributed hoop stress, Newman and Raju [7, 8] developed a two-step estimate method. First, they fit an arbitrarily nonlinear hoop stress on the crack surface using a 3rd-degree polynomial function that contains the uniform, linear, quadratic, and cubic terms. Then, the K factor was calculated using the 3D FEA results as the sum of the four specific K factors that were referred to as the boundary correction factors, G0 for the uniform stress, G1 for the linear stress, G2 for the quadratic stress, and G3 for the cubic stress. However, their FEA results were obtained only for two selected cylinders of t/R_i=0.1 and 0.25. Thus, Anderson et al. [11] performed a large number of 3D FEA calculations for surface cracks in a wide range of cylinder sizes with t/R_i from 0 to 1, and obtained a set of tabular data of G0 and G1 for a variety of surface cracks in the cylinders. These FEA-based tabular data were adopted by API 579 [1]. Delliou and Chapuliot [12] compared the tabular data of K in API 579 with those used in French pressure vessel code RSE-M, and showed that the K solutions in both standards agree satisfactorily. Ceelho et al. [13] performed the case study of surface cracks in cylinders using the advanced 3D FEA simulations, and showed that the tabular data of K in API 579 are generally accurate and adequate to use for the FFS evaluation of pressure vessels. Recently, Li and Hasegawa [14, 15] further obtained the FEA results of K for surface cracks in cylinders with high aspect ratios that are not considered in API 579.

The tabular data of the K factor in API 579 have been obtained extensive applications in the ECA or FFS evaluation of pressure vessels. However, due to discrete data nature, three-parameter interpolations are needed for arbitrary cylinder or crack sizes. Thus, a closed-form solution of stress intensity factor was desired for engineering application. Accordingly, based on the tabular data of the K factor given in API 579, Xue et al. [16, 17] employed the nonlinear regression method, and obtained a set of curve-fit solutions of the influence coefficients G0 and G1 for axial inside and outside semi-elliptical surface cracks for the API selected cylinder sizes. Those closed-form solutions of the K factor are applicable to any crack sizes for API selected cylinder sizes, but interpolations are still needed for other cylinder sizes with an arbitrary R_i/t ratio.

So motivated, this paper attempts to develop a more general solution of K for axial outside surface cracks in pressurized cylinders using the state-of-the-art machine learning technology. Based on the tabular datasets of G0 and G1 given in API 579 for axial outside semi-elliptical surface cracks in thick-wall cylinders at the deepest and surface points, data-driven solutions of K are obtained. The machine learning method utilizes an artificial neural network (ANN), activation function and optimal learning algorithm to learn and to determine a general solution of K as a function of the cylinder size (t/R_i), aspect ratio (a/c), and crack depth (a/t) for an axial outside surface crack at its deepest and surface points. The proposed data-driven solutions of G0 and G1 for the axial outside surface cracks are validated by the curve-fit solutions obtained by Xu et al. [17].

2. TABULAR DATA OF K FACTOR IN API 579

2.1 Engineering estimates of K factor

Consider an axial outside semi-elliptical surface crack in a pressurized cylindrical pressure vessel, as shown in Fig. 1, where R_i is the inside radius of the cylinder, t is the wall thickness, a is the crack depth, c is one half of the crack length and $l = 2c$ is the crack length. In addition, φ denotes the parametric angle of the semi-elliptical crack and $\beta = \frac{2\varphi}{\pi}$ is the normalized parametric angle of the semi-elliptical crack. The parametric angle defines the location of a point of interest at the elliptical crack front. As shown in Fig. 1, Point 1 denotes the deepest point of the crack with $\varphi = \frac{\pi}{2}$ or β=1, and Point 2 denotes the surface point of the crack with φ=0 or β=0.

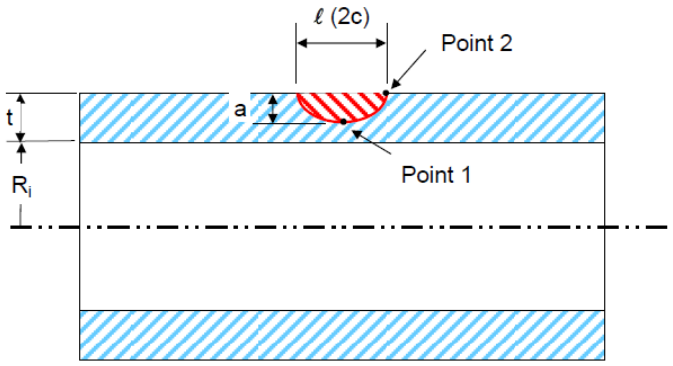

Figure 1: An axial outside semi-elliptical surface crack in a cylinder

As previously introduced, the tabular data of the K that are given in API 579 [1] for surface cracks in cylinders were obtained by Anderson et al. [11] based on their extensive 3D FEA results. These authors adopted the two-step engineering estimate method that was developed by Newman and Raju [7, 8]. At first, the method estimates the representative stress at the crack location, and then the representative stress is used to estimate the corresponding stress intensity factor. Specifically, the first step is to determine the stress distribution at the crack surface location through the stress analysis of the cracked component under an applied loading in absence of the crack, and the actual stress distribution at the crack location is represented by a curve-fit 4th-degree polynomial function that contains the uniform, linear, quadratic, cubic and quartic terms. In the second step, the

representation of the general stress distribution at the crack location is used with the standardized influence coefficients G0, G1, G2, G3 and G4 that are given in API 579 to calculate the K factor for the specific stress on the surface crack in cylinders, where G0, G1, G2, G3, and G4 are four nondimensional stress intensity factors that correspond to the uniform stress, linear stress, quadratic stress, cubic stress, and quartic stress acting on the crack surface, respectively.

These standardized tabular data of the K factor make the engineering estimate method very convenient and efficient to use in estimating the stress intensity factor for surface cracks.

2.2 Polynomial representation of stress distribution

For a thick-wall cylinder subject to a combined loading, the hoop stress should be a nonlinear distribution through the wall thickness. The actual stress at the crack surface location can be accurately curve-fitted to a 4th-degree polynomial function over the wall thickness that is represented in API 579 [1] by:

$$\sigma(x) = \sigma_0 + \sigma_1\left(\frac{x}{t}\right) + \sigma_2\left(\frac{x}{t}\right)^2 + \sigma_3\left(\frac{x}{t}\right)^3 + \sigma_4\left(\frac{x}{t}\right)^4 \quad (1)$$

where $\sigma(x)$ is the representation of actual hoop stress distribution through the wall thickness, x is a local coordinate and measured from the origin on the crack mouth toward the deepest point of the surface crack (see Fig. 1), and σ_j denotes five curve-fit parameters of the polynomial function of general stress distributed on the crack surface. Particularly, $\sigma(0)=\sigma_0$ is the hoop stress on the outside surface of the cylinder, and $\sigma(t) = \sigma_0 + \sigma_1 + \sigma_2 + \sigma_3 + \sigma_4$ is the hoop stress on the inside surface. Those two stresses lead to membrane stress and bending stress at the crack location.

For a thick-wall cylinder subject to internal pressure only, the well-known Lamè hoop stress [1] is:

$$\sigma_{\theta\theta} = \frac{PR_i^2}{R_0^2 - R_i^2}\left[1 + \left(\frac{R_0}{r}\right)^2\right] \quad (2)$$

where R_0 is the outside radius of the cylinder, P is the internal pressure, and r is the polar coordinate in a range of $R_i \le r \le R_0$. Using the local x coordinate, the hoop stress can be approximated by the following Taylor series:

$$\sigma_{\theta\theta} = \frac{PR_i^2}{R_0^2 - R_i^2}\left[2 + 2\left(\frac{a}{R_0}\right)^1\left(\frac{x}{a}\right)^1 + 3\left(\frac{a}{R_0}\right)^2\left(\frac{x}{a}\right)^2 + 4\left(\frac{a}{R_0}\right)^3\left(\frac{x}{a}\right)^3 + 5\left(\frac{a}{R_0}\right)^4\left(\frac{x}{a}\right)^4\right] \quad (3)$$

2.3 Stress intensity factor solutions

For the 4th-degree polynomial representation of the general stress distribution over the crack surface location as expressed in Eq. (1), the corresponding stress intensity factor is calculated using the following equation:

$$K_I = \sum_{j=0}^{4} \sigma_j \left(\frac{a}{t}\right)^j G_j \left(\frac{\pi a}{Q}\right)^{\frac{1}{2}} \quad (4)$$

where a is the crack length, c is one half of the crack length, σ_j is the coefficient of stress representation, G_j is the influence coefficients of K_I that correspond to σ_j, K_I is the stress intensity factor for Model-I cracks, and Q is the surface crack shape factor that was defined by Newman and Raju [7, 8] in the following expression:

$$Q = \begin{cases} 1 + 1.464\left(\frac{a}{c}\right)^{1.65}, & for\ \frac{a}{c} \le 1 \\ 1 + 1.464\left(\frac{c}{a}\right)^{1.65}, & for\ \frac{a}{c} > 1 \end{cases} \quad (5)$$

For a thick-wall cylindrical pressure vessel, using the representative series of the hoop stress in Eq. (1), the stress intensity factor in Eq. (4) becomes:

$$K_I = \left(\frac{\pi a}{Q}\right)^{\frac{1}{2}} \frac{PR_i^2}{R_0^2 - R_i^2}\left[2G_0 + 2\left(\frac{a}{R_0}\right)^1 G_1 + 3\left(\frac{a}{R_0}\right)^2 G_2 + 4\left(\frac{a}{R_0}\right)^3 G_3 + 5\left(\frac{a}{R_0}\right)^4 G_4\right] \quad (6)$$

For axial semi-elliptical surface cracks on the outside surface of cylinders, the tabular data of the influence coefficients G_0 and G_1 in API 579 [1] cover the t/R_i ratios in a wide range of 0 to 1, the a/t ratio in a range of 0 to 0.8, and the a/c ratios in a range of 0.03125 to 2. For axial surface cracks with $a/c = 0$ on the outside surface of cylinders, API 579 [1] covers the Ri/t ratio from 1 to 1000 and the a/t ratio from 0 to 0.8. In API 579, the influence coefficients G_0 and G_1 are expressed in the following 6th-degree polynomial functions of the parametric angle, and the coefficients were obtained by the curve fitting from the FEA results obtained by Anderson et al. [11]:

$$G_0 = A_{00} + A_{10}\beta + A_{20}\beta^2 + A_{30}\beta^3 + A_{40}\beta^4 + A_{50}\beta^5 + A_{60}\beta^6 \quad (7)$$

$$G_1 = A_{01} + A_{11}\beta + A_{21}\beta^2 + A_{31}\beta^3 + A_{41}\beta^4 + A_{51}\beta^5 + A_{61}\beta^6 \quad (8)$$

where A_{ij} are the curve-fit parameters, their values are given in Table 9B.13 in API 579 [1]. Table 1 is an example of a partial Table 9B.13 that gives A_{ij} values for G_0 and G_1 for an axial outside semi-elliptical surface cracks in a thick-wall cylinder, where t/R_i=1, a/c=0.0625 and 0.125, a/t=0, 0.2, 0.4, 0.6 and 0.8. Once the influence coefficients G0 and G1 are obtained, the higher-order influence coefficients G2, G3 and G4 can be determined from G0 and G1 using the weight function approach, see Paragraph 9B.14.3 and 9B.14.4 in API 579 [1] for details. For a thinner wall R_i/t=10, it may be good to use G0 and G1 only.

Table 1. Example of Table 9B.13 – Influence Coefficients for A Longitudinal Semi-Elliptical Surface Crack in A Cylinder – Outside Surface [1]

t/R_i	a/c	a/t	G_i	A_0	A_1	A_2	A_3	A_4	A_5	A_6
1.0	0.0625	0	G_0	0.2695332	2.1626001	-1.6551569	-1.2970208	4.5604304	-4.3163876	1.4010655
			G_1	0.0138667	0.1827458	2.5749608	-3.9044679	3.3556301	-2.1772209	0.6420134
		0.2	G_0	0.2715940	2.1024792	-0.8251686	-2.6055393	5.9209240	-5.2455526	1.6548386
			G_1	0.0150303	0.1758222	2.5677841	-3.6074069	3.1408983	-2.2687756	0.7163039
		0.4	G_0	0.2777113	2.0986556	-0.4194664	-1.4260711	3.5011609	-3.8010267	1.3387712
			G_1	0.0155020	0.1836026	2.6006839	-3.5389388	4.0212185	-3.7247058	1.2977739
		0.6	G_0	0.2851041	2.2337177	-0.4669277	0.8347740	0.8911966	-3.1973040	1.4390293
			G_1	0.0157533	0.2014410	2.5657394	-3.0637200	4.4719504	-4.9446888	1.7843463
		0.8	G_0	0.2969615	2.1296733	1.3452081	-1.8273770	5.4502252	-6.5713644	1.9432135
			G_1	0.0164599	0.1880783	2.8160846	-3.4852155	6.3096325	-6.4218489	1.9105821
1.0	0.125	0	G_0	0.4065238	0.7772483	3.8861644	-12.573943	16.760207	-11.014593	2.8706957
			G_1	0.0320270	0.1825342	2.2670449	-2.7076615	1.2088194	-0.3777430	0.0763155
		0.2	G_0	0.4115155	0.9865037	3.3032079	-11.115382	15.618784	-11.008999	3.0590331
			G_1	0.0376572	0.1690832	2.4719152	-3.5008614	3.1003664	-2.2831015	0.7359275
		0.4	G_0	0.4209793	1.2265337	1.7709653	-4.0978290	4.4536450	-3.1148588	0.8818491
			G_1	0.0464776	0.0297565	3.8704434	-8.3559638	12.050090	-9.9545839	3.1515874
		0.6	G_0	0.4608006	1.0040220	4.4900108	-11.185813	16.857163	-14.057447	4.4135613
			G_1	0.0464015	0.1688809	2.8532660	-4.2870329	6.2310777	-6.0886059	2.0869057
		0.8	G_0	0.4993921	0.7249266	7.4797239	-18.027074	29.219795	-24.705288	7.5136262
			G_1	0.0519622	0.1229523	3.4495151	-6.0021006	10.613460	-10.115804	3.1838115

3. CURVE-FIT SOLUTIONS OF K

API 579 [1] considers infinite and finite axial surface cracks separately. For very long or infinite axial surface cracks, a/c≈0, the surface crack becomes a regular one-dimensional crack that is described by the crack depth only. From the tabular data of G0 and G1 that covers the R_i/t ratio of 1 to 1000 and the a/t ratio of 0 to 0.8, Xue et al. [17] obtained the curve-fit solutions of G0 and G1 as a function of a/t and R_i/t with a high accuracy. This paper will not further consider these kinds of simple cracks.

For finite axial surface cracks, the crack aspect ratio a/c>0, as illustrated in Fig. 1., API 579 [1] provided the tabular data of G0 and G1, as shown in Table 1, for those finite surface cracks with the crack aspect ratio a/c in a range of 0.03125 to 2 and the crack depth ratio a/t in a range of 0 to 0.8. For an analysis of crack initiation, growth, or failure, the ECA analysis only focuses on the deepest and surface points, and the new semi-elliptical surface crack shape will be determined by the crack increments estimated at these two points. As a result, Xue et al. [17] determined the best curve fit of closed-form relation of G1 and G2 from the tabular data at those two points. For ASME Section XI applications, crack depth does not exceed one half of the crack length, *i.e.*, $a/c \leq 1$, and thus Xue et al. [17] utilized API tabular data within these aspect ratios in their curve fitting.

3.1 Data source

The *G0* and *G1* values at the deepest point and the surface point are taken from API 579 [1] for the following cylinder and crack sizes that are used in the curve fitting to obtain the closed-form relations:

- *Seven* R_i/t ratios = 1, 3, 5, 10, 20, 60, 100
- *Five* a/t ratios = 0, 0.2, 0.4, 0.6, 0.8
- *Six* a/c ratios = 0.03125, 0.0625, 0.125, 0.25, 0.5, 1

3.2 Data curve fitting

Because of the extreme complexity and difficulty, Xue et al. [17] did not attempt to use the three-parameter curve-fit approach to obtain closed-form relations of *G0* or *G1* as a function of R_i/t, a/t and a/c ratios. Instead, they utilized the two-parameter curve-fitting approach and obtained a set of closed-form relations of *G0* and *G1* as a function of a/t and a/c ratios for each given R_i/t ratio. During the curve fitting, those authors employed the commercial data fitting software TableCurve2D and SigmaPlot.

3.3 Curve-fit solutions of G0 and G1

Xue et al. [17] reported a set of the curve-fit solutions of G0 and G1 at the deepest and surface points for the API selected cylinders with seven R_i/t ratios = 1, 3, 5, 10, 20, 60, and 100. For each of these cylinders, there are two curve-fit equations for G0 and G1. And so, for the seven cylinders, there are 14 curve-fit equations for G0 and G1. This results in a total of 28 curve-fit equations being developed by those authors.

As an example, the following two curve-fit equations of G0 and G1 at the deepest point are taken from Xue et al. [17] for the cylinder with R_i/t=10 that represents a transition cylinder size between thick-wall cylinders and thin-wall cylinders:

$$G_0 = A_0 + A_1\left(\frac{a}{t}\right)^{1.5} + A_2\left(\frac{a}{t}\right)^{2} + A_3\left(\frac{a}{t}\right)^{3} \tag{9}$$

where

$$A_0 = 1.14 + 0.0019\left(\frac{a}{c}\right)^{-0.5} - 0.078\left(\frac{a}{c}\right)^{0.5} - 0.0084\left(\frac{a}{c}\right)^{1} - 0.0069\left(\frac{a}{c}\right)^{3} \tag{10a}$$

$$A_1 = 2.6 + 0.43\left(\frac{a}{c}\right)^{-0.5} - 19.67\left(\frac{a}{c}\right)^{0.5} + 21.06\left(\frac{a}{c}\right)^{1} - 4.47\left(\frac{a}{c}\right)^{3} \tag{10b}$$

$$A_2 = 2.11 - 1.3\left(\frac{a}{c}\right)^{-0.5} + 29.14\left(\frac{a}{c}\right)^{0.5} - 39.15\left(\frac{a}{c}\right)^{1} + 9.7\left(\frac{a}{c}\right)^{3} \tag{10c}$$

$$A_3 = 11.96 + 0.43\left(\frac{a}{c}\right)^{-0.5} - 56.09\left(\frac{a}{c}\right)^{0.5} + 54.05\left(\frac{a}{c}\right)^{1} - 10.72\left(\frac{a}{c}\right)^{3} \tag{10d}$$

and

$$G_1 = B_0 + B_1\left(\frac{a}{t}\right)^{0.5} + B_2\left(\frac{a}{t}\right)^{1} + B_3\left(\frac{a}{t}\right)^{1.5} \tag{11}$$

where

$$B_0 = 0.7 - 0.397\left(\frac{a}{c}\right)^{1} + 3.876\left(\frac{a}{c}\right)^{2} - 6.63\left(\frac{a}{c}\right)^{2.5} + 3.19\left(\frac{a}{c}\right)^{3} \tag{12a}$$

$$B_1 = 1.96 - 21.12\left(\frac{a}{c}\right)^{1} + 109.9\left(\frac{a}{c}\right)^{2} - 150.3\left(\frac{a}{c}\right)^{2.5} + 59.44\left(\frac{a}{c}\right)^{3} \tag{12b}$$

$$B_2 = -7.86 + 80.32\left(\frac{a}{c}\right)^{1} - 431.1\left(\frac{a}{c}\right)^{2} + 603.4\left(\frac{a}{c}\right)^{2.5} - 244.4\left(\frac{a}{c}\right)^{3} \tag{12c}$$

$$B_3 = 8.77 - 80.07\left(\frac{a}{c}\right)^{1} + 424.5\left(\frac{a}{c}\right)^{2} - 596.4\left(\frac{a}{c}\right)^{2.5} + 243 \tag{12d}$$

Figures 2 and 3 compare the curve-fit results with API 579 tabular data of the influence coefficient G0 and G1, respectively at the deepest point of the surface crack in a pressurized cylinder with $R_i/t=10$. As shown in the figures, the curve-fit results and the API 579 tabular data agree very well. This indicates the curve fitting has a high accuracy. Through detailed comparisons, Xue et al. [17] concluded that the curve-fit results are very accurate for most data points, and the fitting errors are generally within 5% for the closed-form relations of G0 and G1 at the deepest point for all data points. For the closed-form relation of G0 and G1 at the surface point, the fitting errors are within 5% for most data points. There is only one data point for G0 at the surface point with the fitting error larger than 5%. However, there are many data points for G1 at the surface point with the fitting errors larger than 5%, but the absolute G1 values are very small. The largest error is -32.65%. In general, the overall accuracy of the curve fitting results is satisfactory.

Noted that Xue et al. [16, 17] obtained the curve-fit closed-form solutions of the influence coefficients G0 and G1 of the K factor for both axial inside and outside semi-elliptical surface cracks in pressurized cylinders, and sooner those closed-form solutions of K were adopted by ASME BPVC Section XI [2] in its 2021 version. Even so, the closed-from solutions of G0 and G1 can be only used in the ECA for the API selected cylinder sizes, i.e., $R_i/t=1$, 3, 5, 10, 20, 60 and 100. For other cylinder sizes, the one-parameter interpolation is still needed to interpolate G0 and G1 based on the R_i/t ratio. As a result, a more general solutions of the K factor without use of interpolation are still desired for the FFS evaluation of pressure vessels.

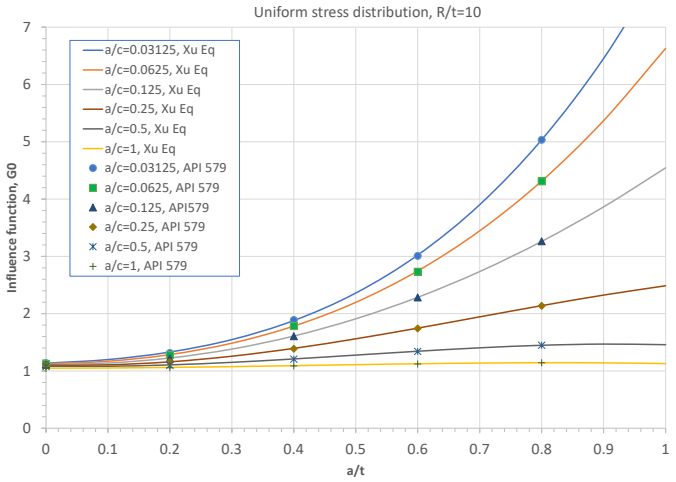

Figure 2: Comparison of curve-fit results with API 579 tabular data of the influence coefficient G_0 at the deepest point for $R_i/t = 10$

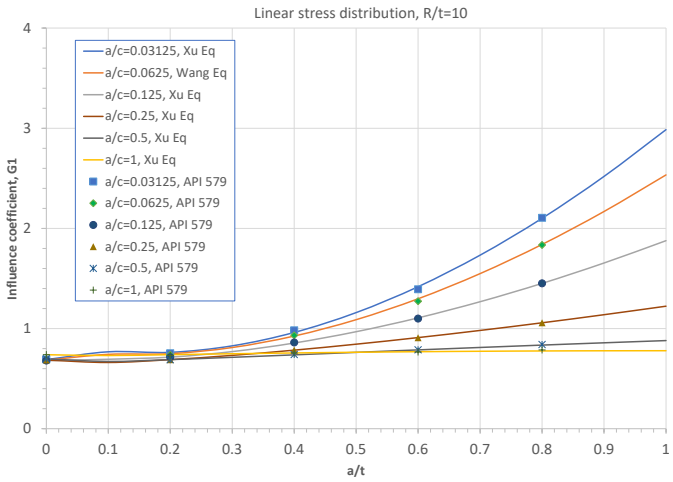

Figure 3: Comparison of curve-fit results with API 579 tabular data of the influence coefficient G_1 at the deepest point for $R_i/t = 10$

4. DATA-DRIVEN SOLUTIONS OF K BY MACHINE LEARNING

4.1 Machine learning method and neural network

To obtain a general solution of the K factor for surface cracks in cylinders without use of interpolation, a data-driven model is developed here using the machine learning technology. Specifically, artificial neural network (ANN) modeling will be used. It is a supervised machine learning approach to learn from previous experience (i.e., labeled input/output data) through built-in learning functions and algorithms, and to make future predictions. A brief technical review on the basic concepts, categories, architectures, activation functions, cost function, model error measures, and modeling procedures of the ANN machine learning approach was given by Zhu et al. [19].

Let's consider a simple ANN model that consists of three layers: input, hidden and output layer. The first layer is an "input layer", which corresponds to independent input variables. The last layer is an "output layer", which corresponds to output variables. The layers between the input and output layers are named as "hidden layers" or a "black box", which contain the hidden neurons. In general, the numbers of both hidden layers and hidden neurons are unknown and are usually determined using the trial-and-error analysis. In many cases, one hidden layer is sufficient for engineering data analyses. In an ANN model, each neuron receives multiple input data, and then adds them through analysis. After that, the combined results are processed with an activation function and a specific algorithm. The value processed by the activation function becomes an output value to other neurons in the next layer or a final output data.

The connection between neurons of different layers is achieved by parametric weights that denote the strength of the connection. Signals received at neuron i can be described by the following combined linear function:

$$u_i = \sum_{j=1}^{N} w_{ij} x_j + b_i \tag{13}$$

And the output data is processed by a transfer function:

$$y_i = f(u_i) \tag{14}$$

where u_i is the linear combined variable from the input data in Eq. (13); $x_1, x_2, \ldots, x_N$ are the independent input variables; N is the total number of input variables; y_i is the dependent output variable of the neuron that can be the final output or the input to another hidden layer; $w_{i1}, w_{i2}, \ldots, w_{iN}$ are the weights of input variables at neuron i; f is an activation function; and b_i denotes a bias. The activation function is needed to introduce nonlinear real-world data to the ANN model. This paper adopts the commonly used sigmoid function, as shown in Fig. 4, to activate connections of neurons between input and hidden layers, whereas a linear activation function is used to activate the connections of neurons between hidden and output layers. The other often used nonlinear activation function is the hyperbolic tangent function and ReLU function.

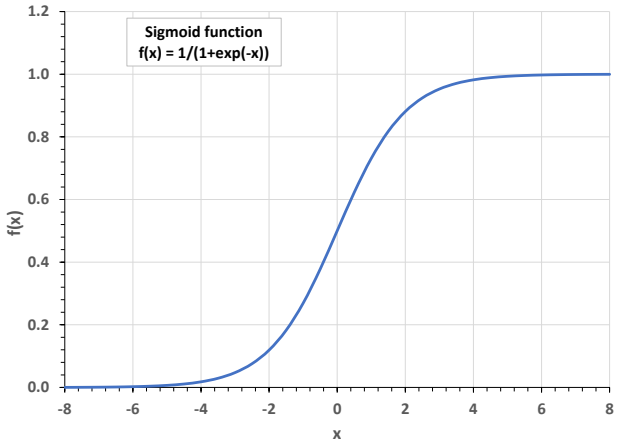

Figure 4: Sigmoid function

During the learning, an initial network architecture is created with an assumed number of hidden layers and hidden neurons and assumed initial random values of weights and biases being applied to the connections. Observation y_i enters the ANN model, and the output $\hat{y}_i$ is obtained. There must be an error between the ANN prediction $\hat{y}_i$ and the real observation y_i. Different indices have been proposed to measure the model error, and the most often used error measure is the root mean squared error (RMSE) in the form of:

$$RMSE = \sqrt{\frac{1}{N}\sum_{i=1}^{N}(y_i - \hat{y}_i)^2} \tag{15}$$

4.2 Construction of ANN model

As discussed in Section 3.1, API 579 [1] provides a large amount of tabular data for the influence coefficients G0 and G1 of the K factor for pressurized cylindrical pressure vessels with seven R_i/t ratios of 1, 3, 5, 10, 20, 60, and 100. In order to obtain a better data-driven model by machine learning, this work only considers thick-wall cylinders with four R_i/t ratios of 1, 3, 5, 10. For each cylinder, six crack aspect ratios are considered as a/c = 0.03125, 0.0625, 0.125, 0.25, 0.5, 1. For each crack aspect ratio, five crack depth ratios are considered as a/t = 0, 0.2, 0.4, 0.6, 0.8. This results in a total of 4x6x5 = 120 data points for G0 or G1 at the deepest or surface point of surface cracks in the thick-wall cylinders that can be extracted from the data tables in API 579 [1]. Since there are only four R_i/t ratios that were considered by API, all four R_i/t ratios or 120 data points are used as training data to develop the ANN models.

The G0 and G1 functions are modeled separately in this work, and each influence coefficient has three input variables: R_i/t, a/c, and a/t, and one output variable: G0 or G1. On this basis, a three-layer ANN model can be constructed, as shown in Fig. 5. In this model, the input layer has three input variables: $x1=R_i/t$, $x2=a/c$, and $x3=a/t$, and the output layer has one output variable y=G0 or G1. One hidden layer with five hidden neurons is assumed based on our previous experience on the similar AAN modelling [19] for predicting the dynamic strength of resistance spot welds in high strength steels. Therefore, this ANN model is simply denoted as 3x5x1. This ANN model contains 20 weights and six biases as marked in Fig. 5. The 120 data points from API 579 are used for this ANN model to learn and to determine the 26 unknown parameters (weights and biases) through iterations. The Excel Solver is utilized to minimize the RMSE error of the cost function, and the 26 unknown parameters take random values as their initial values. Once a minimal RMSE error is reached, the weights and biases are determined from the datasets and the ANN model is completely determined.

Note that the same ANN model as shown in Fig. 5 is used to determine four data-driven models for G0 and G1 at the deepest and surface points of axial elliptical surface cracks in thick-wall cylindrical pressure vessels, as discussed next.

4.3 Data-driven model of G0 at the deepest point

Figures 6(a) and 6(b) compare the ANN model predictions (output data) with the API 579 target data of G0 at the deepest point of axial outside surface cracks for all 120 data points in normalized values and actual values, respectively. These figures show that the ANN predictions agree very well with the API target data at the deepest point, and the goodness-of-fit measure R^2 = 0.9983 for all 120 data points. This indicates that the proposed ANN model is very accurate for predicting the G0 values at the deepest point in comparison to the tabular data given in API 579.

Figures 7(a) to 7(c) compares the ANN predictions with API data of G0 at the deepest point for R_i/t=10, 5, and 3. Again, it is observed that the ANN predictions match well with the API data of G0 for all API cylinders and the model errors for most data points are less than 2%.

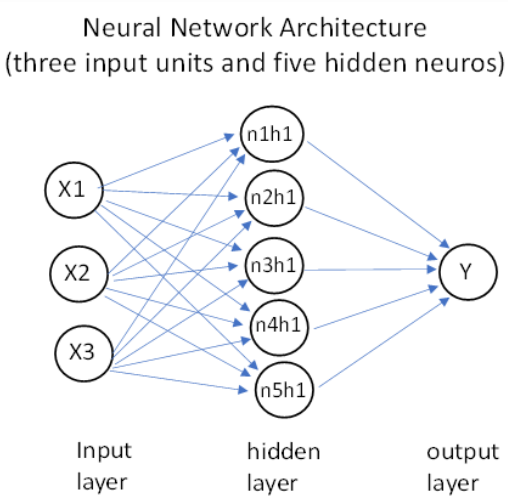

Figure 5: Architecture of ANN model

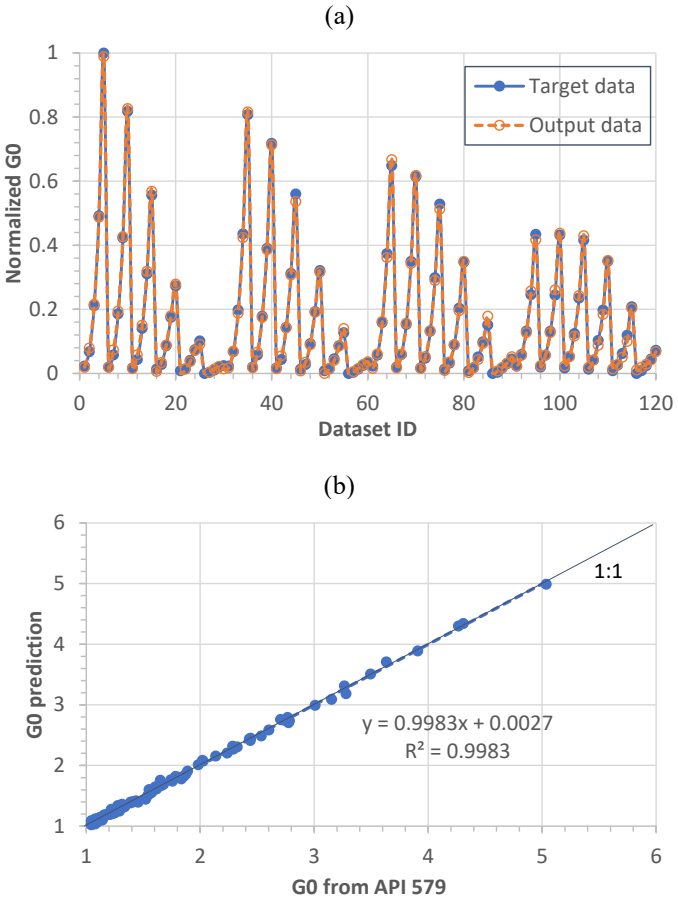

Figure 6: Comparison of ANN model predictions with targe data of G0 at the deepest point from API 579 (a) normalized values, and (b) actual values

(a)

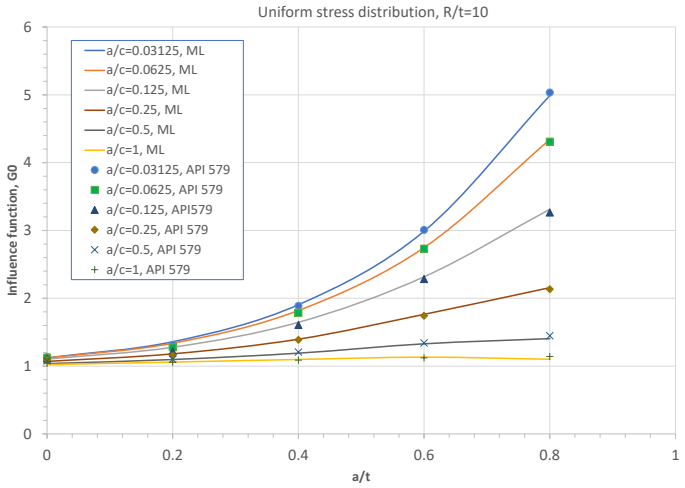

(b)

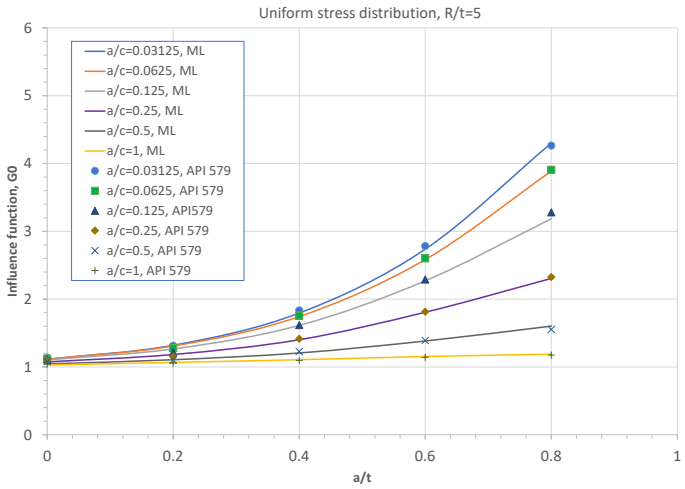

(c)

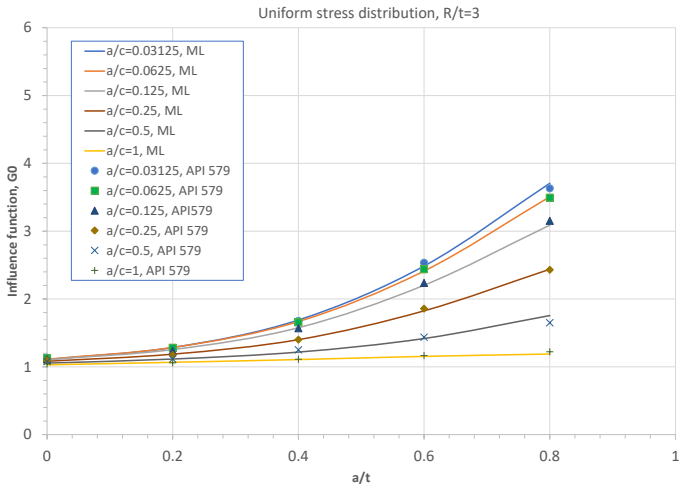

Figure 7: Comparison of ANN predictions with API data of G0 at the deepest point for (a) $R_i/t=10$, (b) $R_i/t=5$, (c) $R_i/t=3$

4.4 Data-driven model of G1 at the deepest point

Figures 8(a) and 8(b) compare the ANN model predictions (output data) with the API 579 target data of G1 at the deepest point of axial outside surface cracks for all 120 datasets in normalized values and actual values, respectively. These figures show that the ANN predictions agree with API given or target data at the deepest point, and the goodness-of-fit measure $R^2 = 0.9975$ for all 120 data points. This indicates that the proposed ANN model is very accurate for predicting the G1 values at the deepest point in comparison to the tabular data given in API 579.

Figures 9(a) to 9(c) compare the ANN predictions with API data of G1 at the deepest point for $R_i/t=10$, 5, and 3. Again, it is observed that the ANN predictions match well with the API data of G1 for all cylinders considered in API 579, and the model errors at most data points are less than 2%.

(a)

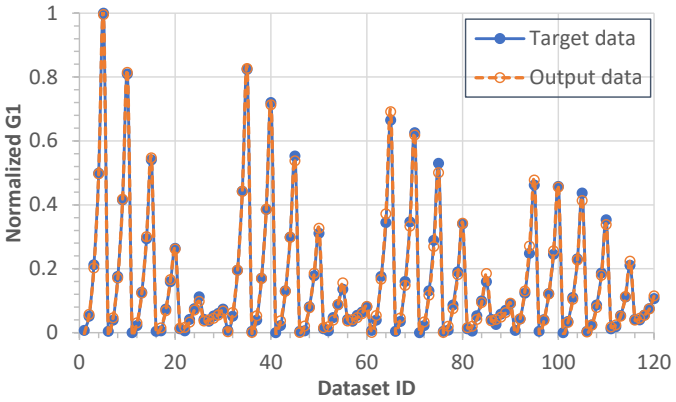

(b)

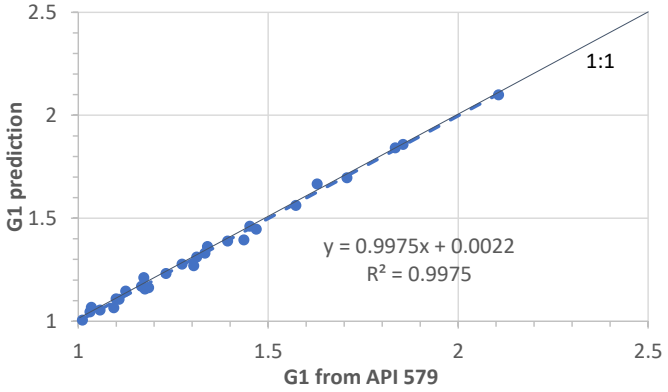

Figure 8: Comparison of ANN model predictions with targe data of G1 at the deepest point from API 579 (a) normalized values, and (b) actual values

(a)

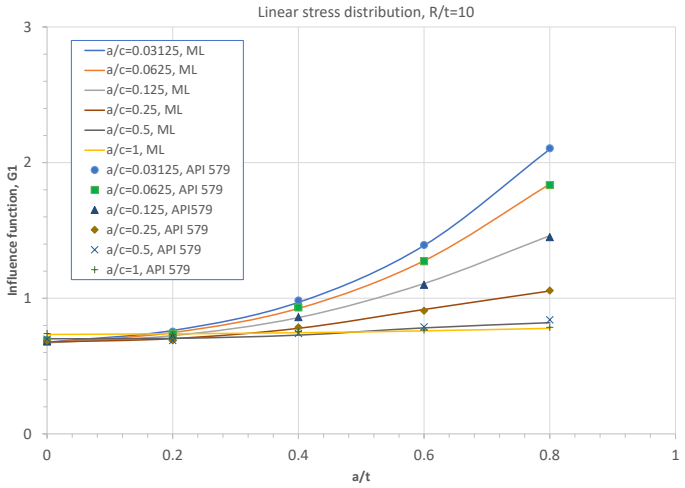

(b)

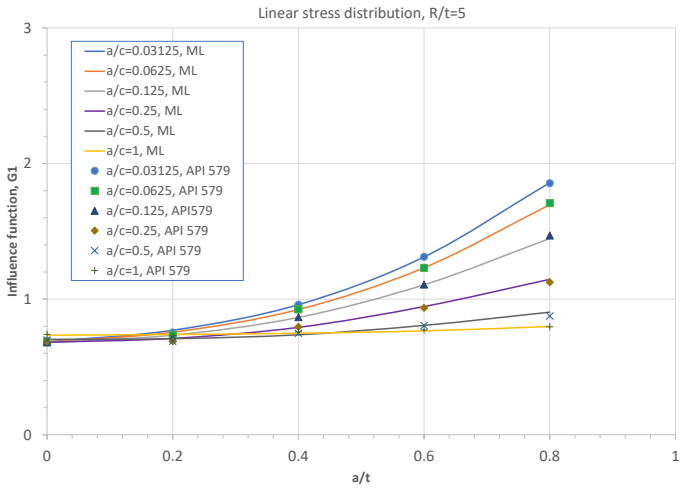

(c)

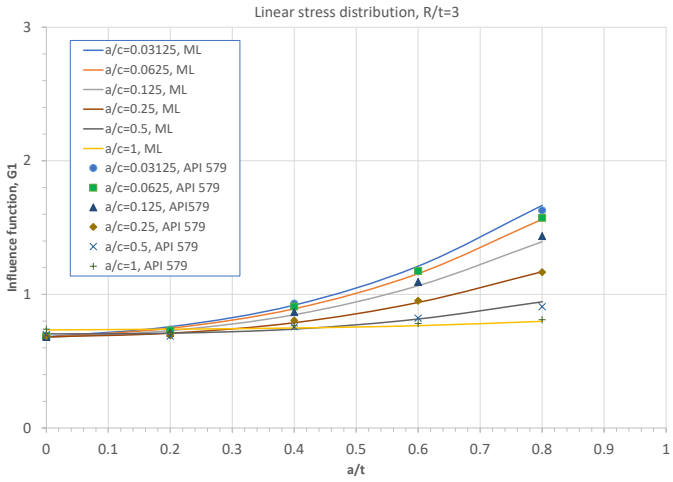

Figure 9: Comparison of ANN predictions with API data of G1 at the deepest point for (a) $R_i/t=10$, (b) $R_i/t=5$, (c) $R_i/t=3$

4.5 Data-driven model of G0 at the surface point

Figures 10(a) and 10(b) compare the ANN model predictions (output data) with the API 579 target data of G0 at the surface point of axial outside surface cracks for all 120 data points in normalized values and actual values, respectively. These figures show that the ANN predictions agree with most of API target data at the surface point, and the goodness-of-fit measure $R^2 = 0.9964$ for all 120 data points. This indicates that the proposed ANN model is accurate for predicting the G0 values at the surface point in comparison to the tabular data given in API 579.

Figures 11(a) to 11(c) compare the ANN predictions with API data of G0 at the surface point for $R_i/t=10$, 5, and 3. Again, it is observed that the ANN predictions match well with the API data of G0 for all cylinders considered in API 579, and the model errors at most data points are less than 5%.

(a)

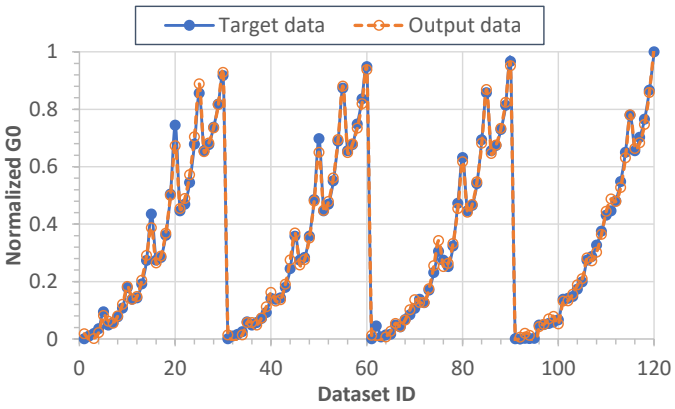

(b)

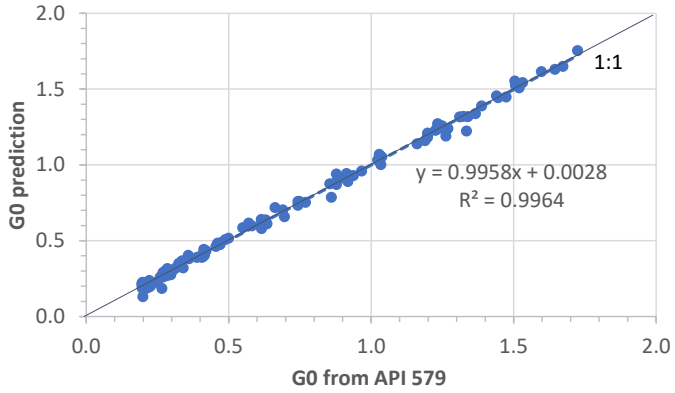

Figure 10: Comparison of ANN model predictions with targe data of G0 at the surface point from API 579 (a) normalized values, and (b) actual values

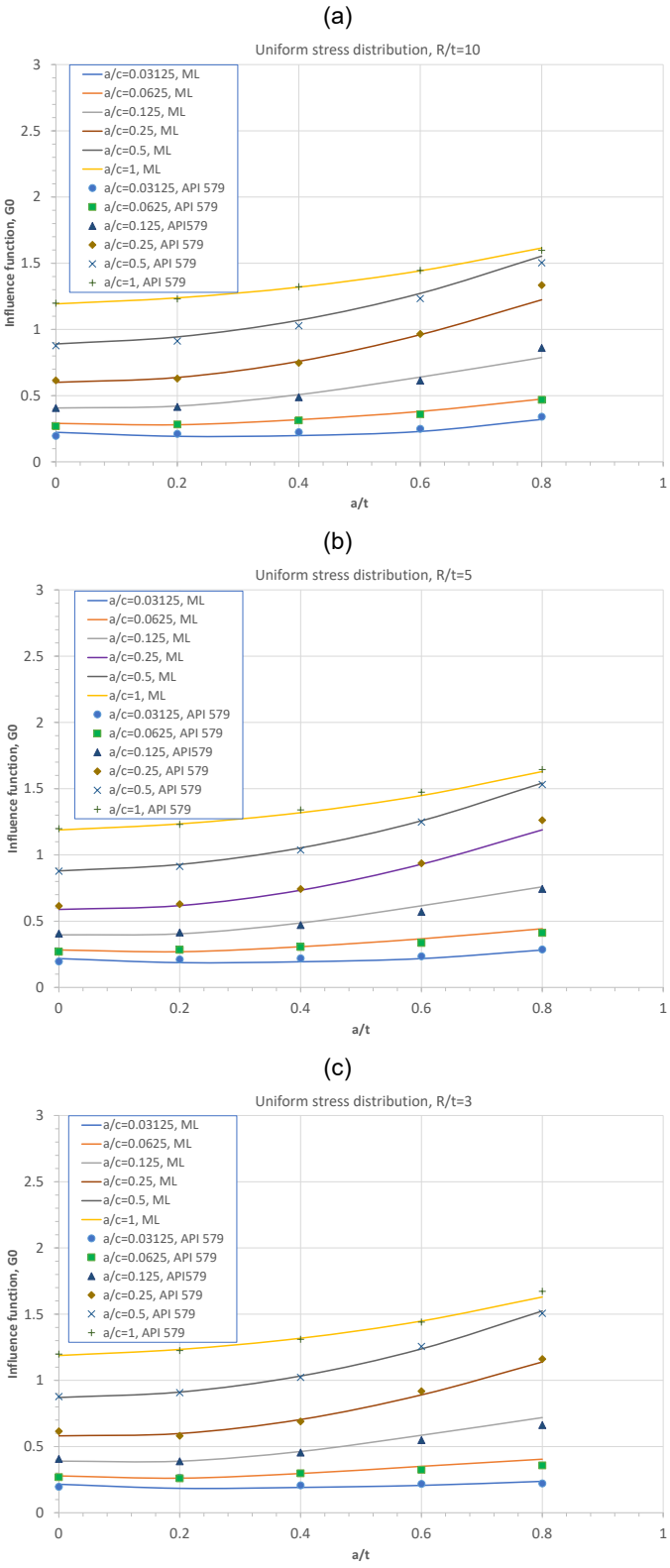

Figure 11: Comparison of ANN predictions with API data of G0 at the surface point for (a) $R_i/t=10$, (b) $R_i/t=5$, (c) $R_i/t=3$

4.6 Data-driven model of G1 at the surface point

Figures 12(a) and 12(b) compare the ANN model predictions (output data) with the API 579 target data of G1 at the surface point of axial outside surface cracks for all 120 data points in normalized values and actual values, respectively. It is shown that the ANN predictions agree with most of API given data at the deepest point, and the goodness-of-fit measure $R^2 = 0.9961$ for all 120 data points. This indicates that the proposed ANN model is accurate for predicting the G1 values at the surface point in comparison to the tabular data given in API 579.

Figures 13(a) to 13(c) compare the ANN predictions with API data of G1 at the surface point for $R_i/t=10$, 5, and 3. Again, it is observed that the ANN predictions match well with the API data of G1 for all cylinders considered in API 579, and the model errors at most points are less 5%.

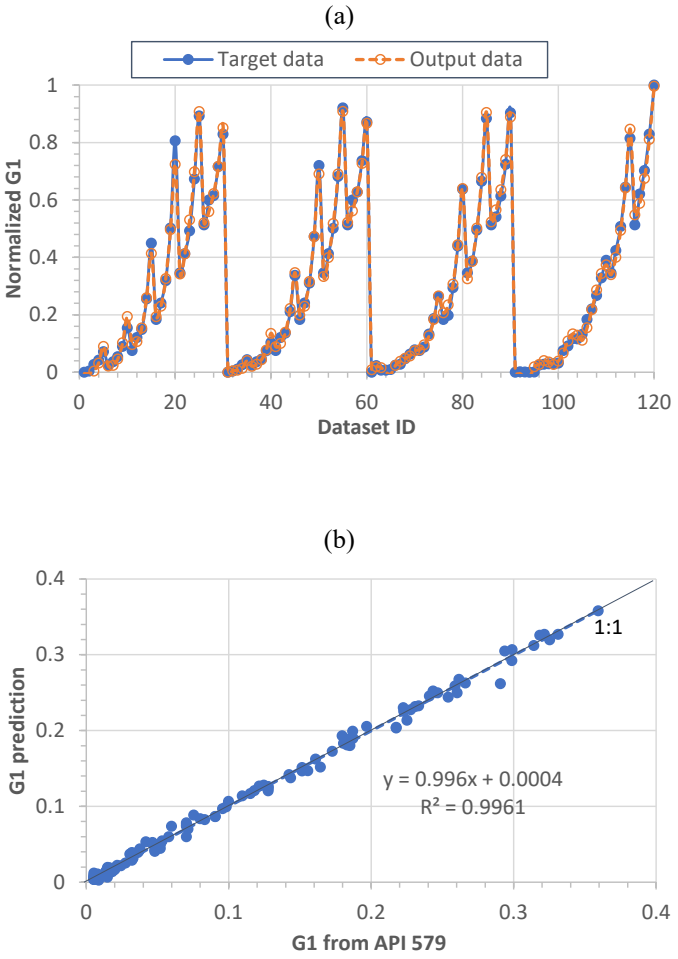

Figure 12: Comparison of ANN model predictions with targe data of G1 at the surface point from API 579 (a) normalized values, and (b) actual values

(a)

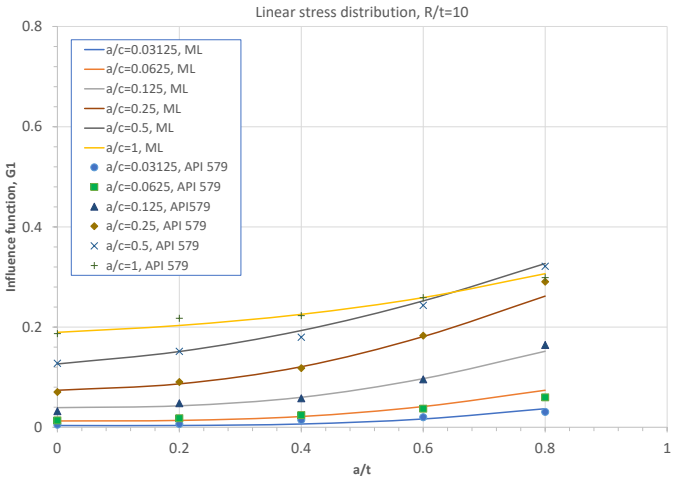

(b)

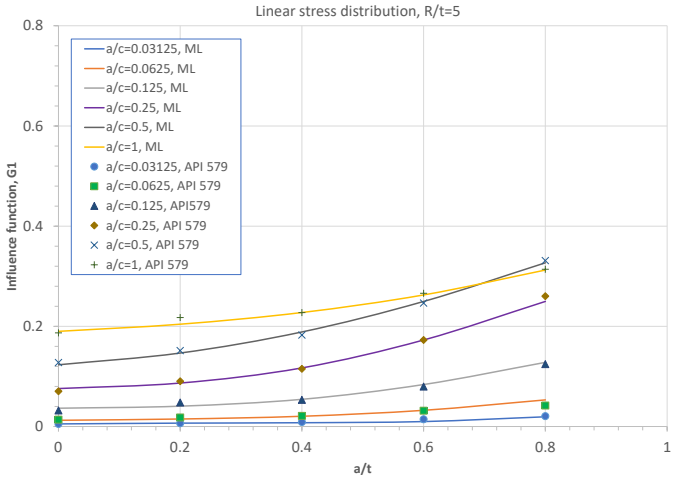

(c)

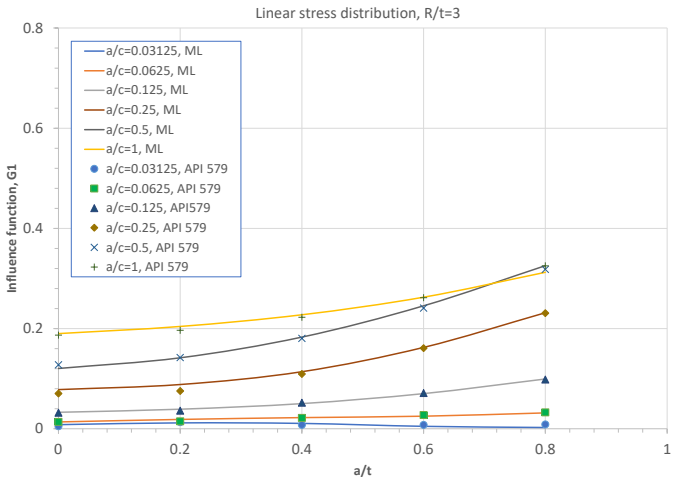

Figure 13: Comparison of ANN predictions with API data of G1 at the surface point for (a) $R_i/t=10$, (b) $R_i/t=5$, (c) $R_i/t=3$

4.7 Validation of ANN models by the curve-fit results

The ANN models of G0 and G1 developed above can be validated using the corresponding curve-fit results obtained by Xu et al. [17]. As shown in Figs 2 and 3, the curve-fit results of G0 and G1 are accurate and nearly identical to the API tabular data for most data points. Likewise, comparisons of the ANN model predictions with the curve-fit results are similar to those shown in Figs 7, 9, 11 and 13. Thus, all ANN models of G0 and G1 are validated by the corresponding curve-fit results.

5. APPLICATION OF DATA-DRIVEN ANN MODEL

As discussed above, four data-driven ANN models of the K factor influence coefficients have been developed for axial outside surface cracks in thick-wall cylinders at the deepest and surface cracks. The detailed comparisons demonstrate that the proposed data-driven models are accurate and adequate to use for the FFS engineering evaluation of pressure vessels.

(a)

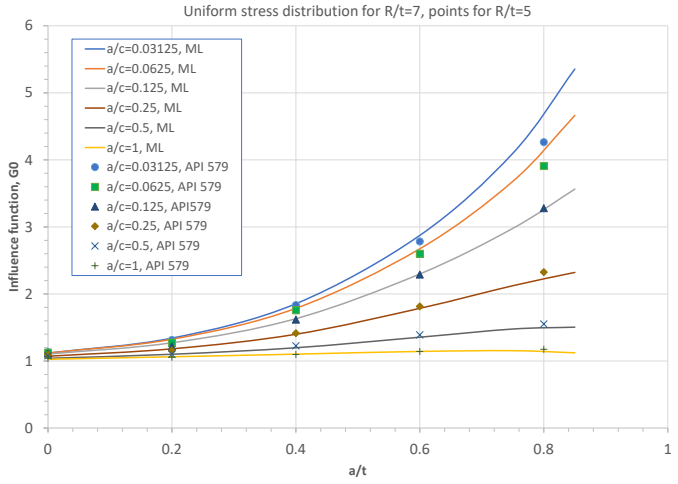

(b)

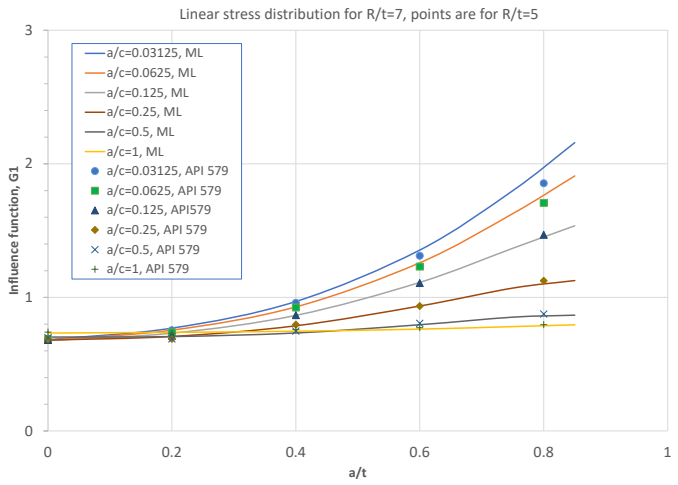

Figure 14: ANN model predictions of influence coefficients at the deepest point of surface cracks for a thick-wall cylinder with $R_i/t=7$ (a) G0, and (b) G1

To demonstrate the capacity of the proposed data-driven models to predict the K factor for any thick-wall cylinder, Figure 14 and 15 show the model predictions of G0 and G1 at the deepest and surface points on elliptical surface cracks in a thick-wall cylinder with $R_i/t=7$, respectively. Also included in those figures are the API tabular data of G0 and G1 for $R_i/t=5$. Comparisons show that all predictions of G0 and G1 for $R_i/t=7$ are reasonable in the trend. With those predicted values of G0 and G1, the K factor are determined, and then a crack growth or instability can be analyzed for that cylinder.

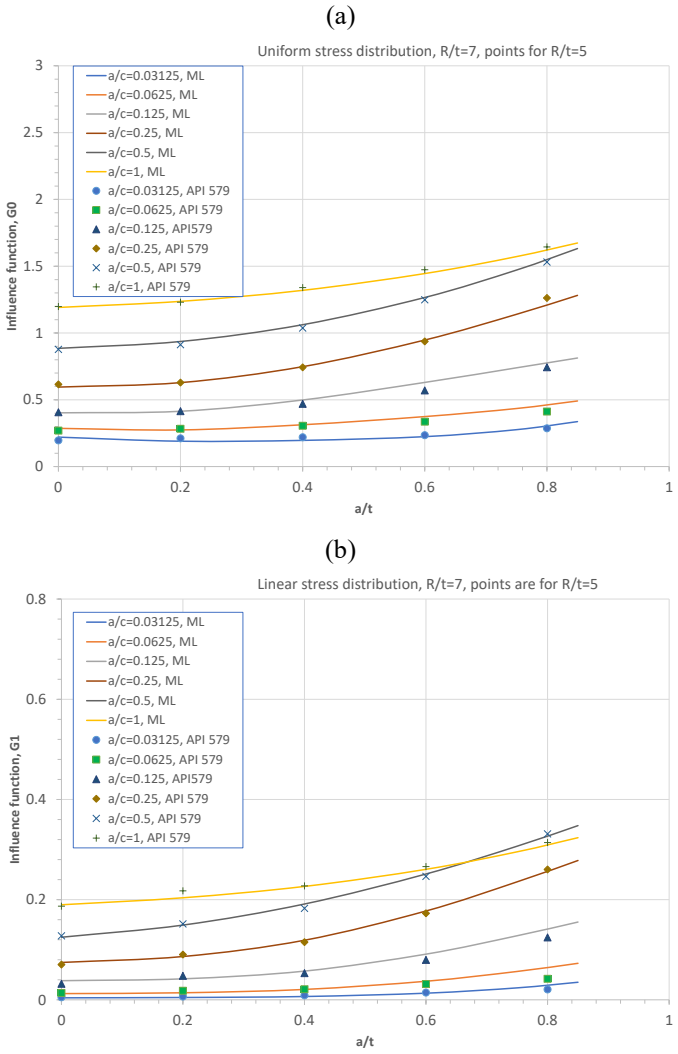

Figure 15: ANN model predictions of influence coefficients at the surface point of surface cracks for a thick-wall cylinder with $R_i/t=7$ (a) G0, and (b) G1

5. CONCLUSIONS

This paper briefly reviewed the tabular data of the stress intensity factor given in API 579 for axial semi-elliptical surface cracks in pressurized cylinders and the corresponding curve-fit closed-form solutions of the influence coefficients G0 and G1 of the stress intensity factor that were obtained by Xu et al. [16, 17] at the deepest and surface points. It was found that the closed-form solutions of G0 and G1 are only applicable to the API selected cylinder sizes. As a result, for any other cylinders that are different from the API cylinder sizes, the interpolations are needed based on the R_i/t ratio. To obtain a more general K solution for any thick-wall cylinder and crack sizes, this paper adopted the machine learning technology and developed four sets of data-driven models of G0 and G1 as a function of the cylinder size (t/R_i), aspect ratio (a/c), and crack depth (a/t) for axial outside surface cracks at the deepest and surface points. From those results, the following conclusions are drawn:

(1) The ANN modeling is an effective machine learning approach used to determine data-driven models of stress intensity factors for the complex 3D surface problems.
(2) The proposed ANN models having three input variables, one hidden layer with five hidden neurons, and one output variable are adequate to use for obtaining accurate predictions of the influence coefficients G0 and G1 in comparison to the API tabular data for axial surface cracks at the deepest and surface points.
(3) The proposed data-driven solutions of G0 and G1 for the axial outside surface cracks are validated by the curve-fit solutions obtained by Xu et al. [17], and thus are adequate to use for predicting the stress intensity factor for the axial surface cracks in thick-wall cylinders.
(4) With the proposed ANN models, one can accurately predict the influence coefficients G0 and G1 and then the stress intensity factor for any axial outside surface crack at the deepest and surface points in a thick-wall cylindrical pressure vessel. Once the stress intensity factor is estimated, the crack growth and instable tearing analysis can be made in an FFS analysis of pressure vessels.

It is noted that the ANN data-driven models were developed based on the all 120 datasets that are available in API 579 for thick-wall pressure vessels as the training datasets, and there are no test datasets used to validate the ANN models built from the training datasets. The proposed ANN models were validated by the curve-fit data obtained by Xu et al. [17] and can be further validated using the 3D FEA results of the stress intensity factor for axial outside surface cracks in any specific cylinder of interest.

ACKNOWLEDGEMENTS

The authors XKZ and AD are grateful to the partial support by the Department of Energy (DOE) and its Laboratory Directed Research and Development (LDRD) program through the LDRD Project 2022-00077 at DOE Savannah River National Laboratory (SRNL).

REFERENCES3

[1] API 579-1/ASME FFS-1, *Fitness-for-Service*, API Publishing Service, June 2016.

[2] ASME Boiler and Pressure Vessel Code (BPVC), 2021 Edition, *Rules for Inservice Inspection of Nuclear Power Plant Components*, Section XI, Division 1, Appendix A.

[3] Underwood J H. "Stress Intensity Factors for Internally Pressurized Thick-Walled Cylinders," *Stress Analysis and Growth of Cracks, ASTM STP 513*, American Society for Testing and Materials, 1972, pp. 59-70.

[4] Kobayashi A S. "A Simple Procedure for Estimating Stress Intensity Factors in Regions of High Stress Gradient," *Significance of Defects in Welded Structures*, eds., T Kanazawa and AS Kobayashi, University of Tokyo Press, 1974, pp. 127-143.

[5] Kobayashi AS, et al. "Inner and Outer Surface Cracks in Internally Pressurized Cylinders," *Journal of Pressure Vessel Technology*, Vol. 99, 1977: 83-89.

[6] McGowan JJ, Raymond M. "Stress Intensity Factor Solutions for Internal Longitudinal Semi-Elliptical Surface Flaws in a Cylinder under Arbitrary Loadings," *Fracture Mechanics, ASTM STP-677*, American Society for Testing and Materials, 1979, pp. 365-380.

[7] Newman JC, Raju IS. "Stress-Intensity Factors for Internal Surface Cracks in Cylindrical Pressure Vessels," *Journal of Pressure Vessel Technology*, Vol. 102, 1980: 342-346.

[8] Raju IS, Newman JC. "Stress-Intensity Factors for Internal and External Surface Cracks in Cylindrical Vessels," *Journal of Pressure Vessel Technology*, Vol. 104, 1982: 293-298.

[9] Wang X, Lambert SB. "Stress Intensity Factors and Weight Functions for Longitudinal Semi-Elliptical Surface Cracks in Thin Pipes," *International Journal of Pressure Vessels and Piping*, Vol. 65, 1996: 75-87.

[10] Akhi AH, Dhar AS. "Stress Intensity Factors for External Corrosions and Cracking of Buried Cast Iron Pipes," *Engineering Fracture Mechanics*, Vol. 250, 2021: 107778.

[11] Anderson TL, et al. "Development of Stress Intensity Factor Solutions for Surface and Embedded Cracks in API 579," *WRC Bulletin 471*, Welding Research Council, New York, May 2002.

[12] Delliou PL, Chapuliot S. "Comparison of the Stress Intensity Factor Influence Coefficients for Axial ID Surface Cracks in Cylinders of RSE-M and API 579-1," *Proceedings of the ASME Pressure Vessels and Piping Conference*, July 19-23, 2015, Boston, MA, USA. PVP2015-45236.

[13] Coelho GC, et al. "Stress Intensity Factor of Semielliptical Surface Crack in Internally Pressurized Hollow Cylinder – A Comparison between BS 7910 and API 579/AME FFS-1 Solutions," *Materials*, Vol. 12, 2019: ma12071042.

[14] Li Y, et al. "Stress Intensity Factors for Cracks with Large Aspect Ratio in Cylinder," Stress Intensity Factor Influence Coefficients for Axial ID Surface Flaws in Cylinders for Appendix A of ASME Section XI," *Proceedings of ASME Pressure Vessels and Piping Conference*, July 14-18, 2013, Paris, France. PVP2013-97665.

[15] Hasegawa K, Li Y. "Development of Stress Intensity Factors for Deep Surface Cracks in Pipes and Plates," *Proceedings of the ASME Pressure Vessels and Piping Conference*, July 19-23, 2015, Boston, MA, USA. PVP2015-45048.

[16] Xu SX, et al, "Closed-form Relations for Stress Intensity Factor Influence Coefficients for Axial ID Surface Flaws in Cylinders for Appendix A of ASME Section XI," *Proceedings of ASME Pressure Vessels and Piping Conference*, July 20-24, 2014, Anaheim, CA, USA. PVP2014-28222.

[17] Xu SX, et al. "Closed-form Relations for Stress Intensity Factor Influence Coefficients for Axial Outside Surface Flaws in Cylinders for Appendix A of ASME Section XI," *Proceedings of ASME Pressure Vessels and Piping Conference*, July 17-21, 2016, Anaheim, CA, USA. PVP2016-64023.

[18] Timoshenko S. *Strength of Materials – Advanced Theory and Problems*, D Van Nostrand Company, New York, 1956.

[19] Zhu JB, Zhu XK, Zhang W. "Machine Learning Modeling of Dynamic Strength of Resistance Spot Welds in High Strength Steels," *Proceedings of ASME Pressure Vessels and Piping Conference*, Virtual Online, July 12-16, 2021, PVP2021-63093.